Experimental validation of the theoretical prediction for the optical S matrix

A. M. Martínez-Argüello,[1] V. Domínguez-Rocha,[1,*] R. A. Méndez-Sánchez,[1] and M. Martínez-Mares[2]

[1]*Instituto de Ciencias Físicas, Universidad Nacional Autónoma de México, Apartado Postal 48-3, 62210 Cuernavaca, Mor., Mexico*
[2]*Departamento de Física, Universidad Autónoma Metropolitana-Iztapalapa, Apartado Postal 55-534, 09340 Ciudad de México, Mexico*

Scattering of waves is present in many areas of physics. Within all these areas, in a great number of systems, the scattering can be separated in an averaged response that crosses rapidly the scattering region and a fluctuating delayed response. This fact is the basis of the optical model; the averaged response, represented by the optical matrix $\langle S \rangle$, is combined with the fluctuating part that can be taken as a random matrix. Although the optical model was developed more than 60 years ago, a theoretical prediction for the optical matrix was obtained only very recently. The validity of such a prediction is experimentally demonstrated here. This is done studying the scattering of torsional waves in a quasi-1D elastic system in which a locally periodic system is built; the full distribution of the scattering matrix is then calculated completely free of parameters. In contradistinction to all previous works, in microwaves and in elasticity, in which the value of $\langle S \rangle$ is obtained from the experiment, here the theoretical prediction is used to compare with the experiment. Numerical simulations show that the theoretical value is still valid when strong disorder is present. Several applications of the theoretical expression for the optical matrix in other areas of physics are proposed. Possible extensions of this work are also discussed.

I. INTRODUCTION

Commonly, in wave scattering at a single frequency, wave amplitudes are separated as reflection and transmission amplitudes. In contradistinction, when a wave packet with multiple frequencies is scattered by a more complex system, the wave amplitudes are divided in a different way: in a prompt response, proportional to the incoming wave packet, which is reflected (or crosses) rapidly the scattering region plus a delayed response that fluctuates in time due to multiple reflections in the different parts of the scattering system. In fact, in many experiments, the reflection and transmission amplitudes are obtained from the prompt response whereas the delayed response has a lot of information used mainly for time reversed signal processing methods [1]. The delayed fluctuating response averages to zero in the time domain, equivalently in energy or frequency, whereas the prompt response quantifies the remaining average that has very slow or null variation in time, energy, or frequency.

This separation of the scattering amplitudes in a component passing rapidly through the scattering region plus a delayed response coming from multiple scattering is summarized in the optical model: dispersion amplitudes are separated into an averaged part and a fluctuating part. The averaged response, on the one hand, is characterized by the optical matrix $\langle S \rangle$, where the average is taken with respect to energy (frequency). Fluctuations, on the other hand, are commonly studied using statistical techniques from random matrix theory. The optical matrix has become therefore a fundamental quantity in the description of multiple scattering of particles and waves. It was introduced in the optical model of the nucleus developed in the 1950's by Feshbach, Porter, and Weisskopf [2,3]. Since the scattering of a nucleon by an atomic nucleus is equivalent to the theory of waveguides [4], this model has been extended not only to chemical reactions but also to electronic transport through ballistic quantum dots and microwave cavities [5,6] and more recently to mechanical waves [7,8].

The average $\langle S \rangle$ can be physically interpreted as the fraction of the incident wave packet which comes out promptly from the scattering region [2]. A concrete realization of $\langle S \rangle$ was proposed in Ref. [9] in the transport of electrons through mesoscopic systems: when the incoming and outgoing channels are not coupled perfectly to the internal system, the optical matrix $\langle S \rangle$ quantifies the coupling between the internal and external regions. This is very important because the imperfect coupling has to be taken into account in almost all scattering experiments [7,10–16].

On the one hand, there are several theoretical studies in which $\langle S \rangle$ is used to obtain the distribution of the scattering matrix known as Poisson's kernel [17–20]. In the one channel case it is univocally determined and reads

$$p_{\langle S \rangle}(S) = \frac{1}{2\pi} \frac{1 - |\langle S \rangle|^2}{|S - \langle S \rangle|^2}, \tag{1}$$

where $S = e^{i\theta}$. The distribution of the S matrix, given by Eq. (1), depends only on $\langle S \rangle$. It is obtained under the hypothesis that, apart of S being unitary, S is an analytic function in the upper half plane of energy from which it is obtained that the kth power $\langle S^k \rangle = \langle S \rangle^k$ which in turn yields into Eq. (1) [6,17].

---
*Present address: Departamento de Física, Universidad Autónoma Metropolitana-Iztapalapa, Apartado Postal 55-534, 09340 Ciudad de México, Mexico.

Furthermore, as a consequence of the analyticity of the S matrix, even when absorption is present [21,22], wave scattering systems are self-averaging [6], which means that the full distribution can be calculated in terms of $\langle S \rangle$, the only relevant parameter needed to obtain all scattering properties in complex systems. This is because the fluctuations seem to be universal only depending on very general symmetry properties as presence/absence of time reversal invariance, among others.

An analytical prediction for $\langle S \rangle$ was obtained only very recently for a one-dimensional chain of delta potentials open at one side only [23], and open at both sides [24]. On the other hand, up to now, there are no experimental studies about $\langle S \rangle$. In all experiments performed in microwave cavities and graphs, and in elastic systems, the value of $\langle S \rangle$ was obtained afterwards from the measurements because an analytical expression for it was not available at that time. Then, to compare with the experiment, the numerical value obtained from the experiment is used in the theoretical expression of Poisson's kernel in a kind of self-consistent argument.

Because the experiment is the only mechanism to validate a theoretical development, in this paper, using elastic waves, the validity of the theoretical prediction for the optical matrix $\langle S \rangle$ given in Ref. [23] is experimentally demonstrated. To do this the scattering of torsional waves in a beam through a finite crystalline structure, machined in a beam, is studied. In contradistinction with the methods of Refs. [25,26], here, to obtain the optical matrix in this system, the scattering formalism developed in Ref. [27] is applied to an elastic crystalline structure. As we are going to see below the distribution of the scattering matrix, with the theoretical value of $\langle S \rangle$, correctly predicts the results measured with acoustic resonant spectroscopy completely free of parameters. Numerical results when disorder is present, are also given.

II. SCATTERING BY A ONE-DIMENSIONAL LOCALLY PERIODIC ROD

Lets consider the semi-infinite beam of Fig. 1(a) in which a locally periodic structure of N notches is machined, such that the unit cell is formed by two parts or bodies labeled as 1 and 2. Plane waves are sent to the structure from the uniform part and the response of the system is obtained using the scattering matrix formalism. The stationary solution $\psi_j(x)$ of the one-dimensional wave equation describing torsions, in the jth body of the unit cell of Fig. 1, is a superposition of waves traveling to the left and to the right $\psi_j(x) = a_j e^{-ik_j x} + b_j e^{ik_j x}$, where $j(=1,2)$ indicates the corresponding part of the unit cell and k_j is the wave number related to the frequency by $k_j = 2\pi f/c_j$ with $c_j = \sqrt{G\alpha_j/\rho I_j}$ the phase velocity of the torsional waves. Here, ρ is the density of the rod, G its shear modulus, I_j the polar moment of inertia of part j, and α_j the Navier series,

$$\alpha_j = \sum_{m=0}^{\infty} \sum_{p=0}^{\infty} \frac{256/\pi^6}{(2m+1)^2(2p+1)^2} \frac{h_j w_j}{\left(\frac{2m+1}{h_j}\right)^2 + \left(\frac{2p+1}{w_j}\right)^2}, \quad (2)$$

with w_j and h_j the width and height of body j.

The boundary conditions between bodies 1 and 2, which are in contact at a point $x = x'$, are continuity of the wave
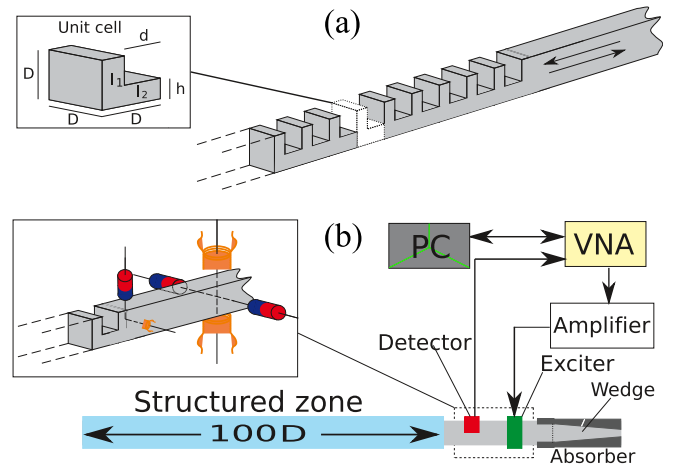
FIG. 1. (a) Aluminum beam ($\sqrt{G/\rho} = 3104.7$ m/s) that consists of a region with a locally periodic structure, composed of N scatterers, and a semi-infinite uniform region of squared cross-section. The unit cell (inset) of length D consists of bodies 1 and 2 of lengths $D - d$ and d, with polar moments of inertia I_1 and I_2, respectively. We use $w_1 = h_1 = w_2 = D = 2.54$ cm, $h_2 = h = 0.9525$ cm and $d = 1.5875$ cm. (b) Setup: a beam consists of a structured zone, a wedge zone with an absorber, and a free region where the exciter and detector are located. (Inset) The coils of the EMAT exciter are connected in series and their polarity is such that the EMAT excites only torsional waves. The EMAT detector is composed of a magnet and a small coil.

amplitude and continuity of the moment of torsion,

$$\psi_1(x') = \psi_2(x'), \quad M_{T_1}(x') = M_{T_2}(x'), \quad (3)$$

respectively. The latter is related to the derivative of the wave amplitude through $M_{T_j}(x) = G\alpha_j \partial\psi_j(x)/\partial x$. Thus the derivative of the wave amplitude, at the point $x = x'$, is discontinuous by a factor $\eta = \alpha_2/\alpha_1$ when the same material is used in bodies 1 and 2. Since the two parts of the unit cell oscillate with the same frequency, the wave numbers of both bodies are related through $k_1 = k_2 c_2/c_1 = k_2 \sqrt{\eta I_1/I_2}$, where $I_1 = \frac{1}{6}D^4$ and $I_2 = \frac{1}{6}D^4(2\frac{h}{D} - 3\frac{h^2}{D^2} + 2\frac{h^3}{D^3})$ are the polar moments of inertia of bodies 1 and 2, of the unit cell of length D, respectively. To calculate I_2, the parallel axes theorem was used with a distance $(D - h)/2$.

The reflection and transmission amplitudes through a single scatterer are

$$r_n = \frac{2i\beta \sin(k_2 d)}{\beta^2 e^{ik_2 d} - e^{-ik_2 d}}, \quad \text{and} \quad t_n = \frac{\beta^2 - 1}{\beta^2 e^{ik_2 d} - e^{-ik_2 d}}, \quad (4)$$

where $\beta = (k_1 - \eta k_2)/(k_1 + \eta k_2)$ and d is the scatterer length. These were obtained using the boundary conditions at both sides of the notch, solving the resulting system of equations. The response of the system of N scatterers is described by the 1×1 scattering matrix S_N, which is related to the scattering matrix S_{N-1} that describes the system with $N-1$ scatterers, through the following recurrence relation [27]:

$$S_N = (r_n z_n^* + z_n S_{N-1})(r_n^* z_n + z_n^* S_{N-1}^*)^{-1} S_{N-1}^*, \quad (5)$$

where $z_n = t_n e^{ik_1(D-d)}$. The wave number k_1 is the tunable parameter, proportional to the frequency, since the uniform
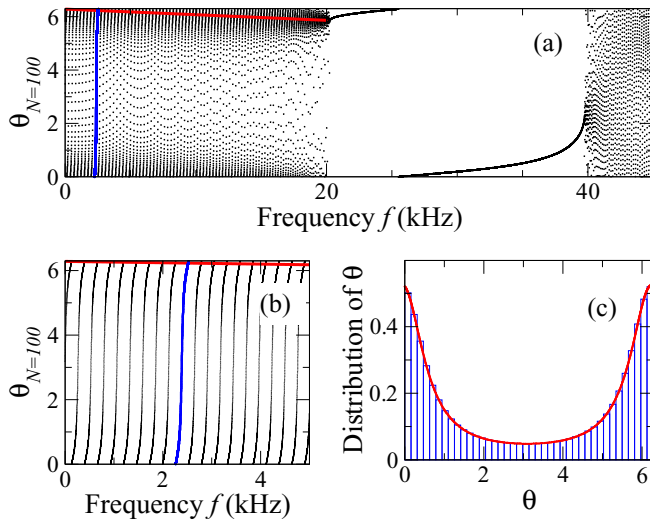
FIG. 2. (a) Phase of the scattering matrix, Eq. (5), as a function of the frequency, for $N = 100$, is shown. The red line corresponds to the phase of the optical matrix $\langle S \rangle$ given in Eq. (6). (b) Zoom of panel (a) for low frequencies. (c) Histogram of the resonance highlighted in blue in (b). The (red) curve is Poisson's kernel (1) with the optical matrix $\langle S \rangle$ taken from Eq. (6).

part of the beam has the same cross-sectional area as body 1 of the unit cell. The scattering matrix given in Eq. (5) can be studied in two different ways: (a) at a fixed k for an ensemble of systems with different values of N and (b) varying k for a single system with a fixed value of N. For case (a), Eq. (5) is interpreted as a nonlinear mapping that accepts stable and unstable fixed point solutions when $N \to \infty$, the latter being a set of zero measure that is ignored. The fixed point solution can be interpreted as the optical matrix, $\langle S \rangle$, because it satisfies the analyticity condition $\langle S^N \rangle = \langle S \rangle^N$ [23] that implies Poisson's kernel. The value of the optical matrix in an allowed band is (the main interest is on the first band only)

$$\langle S \rangle = i(r_n^* z_n)^{-1}[-\sqrt{|t_n|^4 - (\text{Re } z_n)^2} + \text{Im } z_n]. \quad (6)$$

It is remarkable that the optical matrix $\langle S \rangle$ and Poisson's kernel, Eq. (1), are completely determined (and only depend) on the values of the reflection and transmission amplitudes of a single scatterer, no matter how they are obtained, by numerical or experimental methods or by a theoretical model as in Eq. (4). In what follows we will focus on case (b) while case (a) is discussed further in Appendix A.

In Fig. 2(a), the phase θ_N is plotted, as a function of the frequency, for $N = 100$. The allowed bands, on the one hand, are observed as regions in which the phase varies rapidly with the frequency. This is due to the fact that in wave systems with one lossless port, i.e., only one incoming channel and outgoing on the same channel, the scattering matrix reduces to a complex number of modulus one $S = e^{i\theta}$. This means that the reflection coefficient is always 1 and the resonances can only be observed in the phase θ when it gives a fast turn on the unit circle; θ is closely related to the phase shift. The gaps, on the other hand, are regions in which the phase presents a slow variation with the frequency. As can

be observed in the same figure, the first band starts at 0 Hz and finishes at approximately 20 kHz; the second band starts around 39.735 kHz. Then the gap is roughly located in the interval (20 kHz, 39.735 kHz). A zoom of the highlighted resonance shown in Fig. 2(a) is given in Fig. 2(b). As it can be seen in this figure, the phase has a variable speed $d\theta/dk$ in the unit circle; the largest slope is associated to the resonances. The fast turn of the phase in each resonance can be quantified by the histograms that measure the number of points that the phase θ falls in the interval $(\theta, \theta + d\theta)$. In Fig. 2(c), the histogram of the phase for the resonance centered at $f = 2395$ Hz, (blue) highlighted in Fig. 2(b), is given; the maximum of the distribution corresponds to the lowest slope of the phase of the resonance. Also, in Fig. 2(c), the distribution of Poisson's kernel, given by Eq. (1) with the average of the scattering matrix $\langle S \rangle$ of Eq. (6) for $f = 2395$ Hz, is plotted. An excellent agreement between the numerical histograms and the theoretical distribution is obtained.

III. EXPERIMENTAL VALIDATION OF THE OPTICAL MATRIX

In what follows we show that Poisson's kernel, with the average taken from Eq. (6), correctly predicts the experimental distribution of the scattering matrix in elastic waves. This will be done for a system with a large, but fixed, number of scatterers within a small frequency range in the first allowed band. The experimental setup is shown in Fig. 1(b). A signal of frequency f, produced by a vector network analyzer (VNA, Anritsu MS-4630B) and intensified by a Cerwin-Vega (CV-900) high-fidelity audio amplifier, is sent to an electro-magnetic acoustic transducer (EMAT) designed ad hoc for this experiment because high power and selectivity is needed. This transducer, composed by two coils and two permanent magnets, shown in the inset, produces torsional vibrations that propagate through the system [28,29]. The response, measured by another EMAT, is directly sent to the VNA. The measurements, amplitude and phase, as a function of the frequency f, are taken from the VNA to the computer through a GPIB port.

The system under study consists of an aluminum beam of squared cross-section of width $D = 2.54$ cm and length 3.6 m divided in three regions. From a free boundary, a locally periodic structure, composed of 100 equal notches as in Fig. 1(b), is machined. The middle part of the beam, of 56 cm length, remains uniform. In this part the waves are excited and the scattering matrix is measured. The other end simulates a semi-infinite beam by means of a passive vibration isolation (PVI) system that absorbs the incoming waves [7,8,30,31]. The PVI system, is composed of a wedge and polymeric foams and has a length of 50 cm, covering completely the wedge and part of the uniform section of the beam. This system allows the measurement of the mechanical scattering matrix, in the frequency domain, since the normal modes of the complete beam cannot be established.

In Fig. 3, the measured amplitude (a) and phase (b) of the scattering matrix, as a function of the frequency, for a part of the first band, is shown. As expected, several resonances of the allowed band, for which the phase takes values between
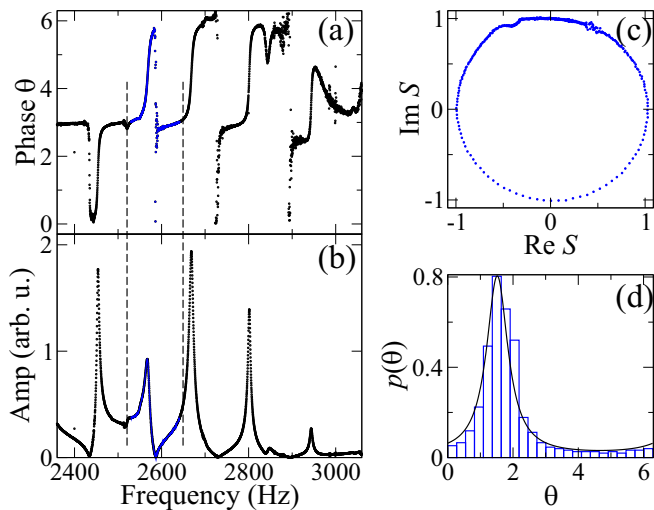
FIG. 3. Amplitude (a) and phase (b) of the *S* matrix as a function of the frequency. Shifted and normalized *S* matrix in the Argand plane (c), in a part of the allowed band. The histogram of the highlighted resonance (blue) at $f = 2570$ Hz and its comparison to Poisson's kernel, Eq. (1) with $\langle S \rangle$ given by Eq. (6), is shown in (d). The dimensions of the unit cell are the same as in Fig. 1 but *h* replaced by an effective value, 0.746*h*, due to the punching of body 2 [28].

FIG. 4. (a) Measured amplitude (in arbitrary units) as a function of the frequency. The analyzed resonances (b), (c), (d), and (e), and their respective histograms (f), (g), (h), and (i), are taken in the intervals (3244.0, 3399.0) Hz, (4859.8, 5019.8) Hz, (5792.0, 5998.0) Hz, and (9560.0, 9760.0) Hz, respectively. The continuous line in the lower panels is Poisson's kernel, Eq. (1), with $\langle S \rangle$ given by Eq. (6).

0 and 2π, are observed. All of these resonances describe, in the Argand plane, nonconcentric circles of different radii. This is due to the impedance of the detector [7,8]. We analyze the phase of the resonance lying between the dotted lines, from 2530.0 to 2638.8 Hz, using the method of Ref. [7] to subtract the shift due to the impedance. As seen in Fig. 3(c), this corrected *S* matrix describes a circle centered at the origin (the radius was set to 1 for convenience). The distribution of the phase along the circle is shown in Fig. 3(d) as a histogram. In the same figure the analytical distribution expressed by Poisson's kernel, Eq. (1), continuous line, is also given. The value of the optical matrix was taken from Eq. (6) and evaluated at $f = 2570$ Hz, the center of the resonance and corrected as described below. One can notice that the maximum of the histogram is located at a different position that in the theoretical result. This shift comes from a global phase that appears in the experiments. The location of the peak depends on which face of the beam the detector is located: measurements in adjacent faces produce a global phase of $\pi/2$ and the histogram will be shifted by this quantity. Also, the maximum of the experimental distribution is larger than the maximum of the numerical distribution of Fig. 2(c). This is due to the fact that a better approximation, using a punching parameter ζ, to calculate r_n and t_n, was used [28]. As it can be seen in Eqs. (2) to (4) the model used for the scattering matrix is 1D while the machined beam is 3D. The punching occurs when two elastic bodies of different cross-sectional area are in contact and subject to a torque (force or bend); in this case Eqs. (3) are meaningless. However, these equations can be corrected: for small torsions the body with smaller area twists nonuniformly the area of the larger body. This extra twist is called "punching" and the coefficient ζ takes into account the punching of body 1 by body 2. This coefficient has been

measured in several cases and, for torsional waves, gives a corrected or effective value of $h_{\text{eff}} = h/(1 + \zeta/d)^{1/4}$, that can be used in Eqs. (2) and (3) with $\zeta = 0.54$ mm. More details of the punching can be found in the Appendix of Ref. [28]. Then, taking into account the global phase and the punching, a very good agreement between theory and experiment is observed.

IV. ROBUSTNESS AGAINST DISORDER, LOSSES, AND SIGNAL-TO-NOISE RATIO

Now the robustness of the expression of the optical matrix, with respect to losses and noise will be addressed; the effects of the disorder are studied numerically in Appendix B and validate the robustness of the optical matrix prediction against disorder. The effect of the losses in the optical matrix prediction can be obtained directly from the experiment since absorption is always present. Contrary to the case in chaotic systems [12,32], in which a generalization of Poisson's kernel appears, in the beam worked here the absorption only gives a shift that can be taken into account in the normalization as in Refs. [7,8,22]. In Fig. 4(a), the measured amplitude, within the first passband, as a function of the frequency, is given. As it can be seen in panels (f) and (g) of the same figure, regardless of the location of the resonance within the allowed band, the agreement between Poisson's kernel, Eq. (1), and the experimental results is excellent. As it can be seen roughly in panel (a) of this figure, as frequency increases the signal becomes smaller. This is evidenced in panels (b), (c), (d), and (e), in which the measured *S* is plotted for the resonances highlighted in panel (a), with the same order. When approaching the forbidden band the signal becomes weak and noisy, panels (d) and (e). Then *S* does not lie in

a circle anymore but it lies in a ring. This effect produces a diminishing of the optical matrix, $\langle S \rangle$, that tend to flatten the distribution, panels (h) and (i), in a similar way that in the disordered case shown in Appendix B.

V. CONCLUDING REMARKS AND OUTLOOK

The good agreement observed between the theory and the experiment represents the validation of the analytical expression of the optical matrix $\langle S \rangle$ through the invariant density of the phase of the S-matrix, Poisson's kernel, that results from a non trivial relation between coherent transport and deterministic maps [33]. The detected torsional waves outside the locally periodic system, a square cross-section beam with 100 notches, correspond to the 1×1 scattering matrix S once they are excited outside of the cavity. The measured distribution of the phase of S of a single resonance agrees with Poisson's kernel using the theoretical prediction given in Eq. (6); the optical matrix given in that equation depends only on (i) the S-matrix composition rule and (ii) the reflection and transmission coefficients of a single unit cell. Thus the prediction for the optical matrix is quite general, with details depending on the constituents of the particular system, and Eq. (6) can be applied to a plethora of wave systems of different nature just having the reflection and transmission of a single scatterer. Several applications are expected in different areas since there are many realizations of a semi-infinite one-dimensional periodic system composed by two media, i.e., a photonic crystal, a superlattice, a layered media in geology, etc. In fact data of the microwave ring, used to measure the transmission through a locally periodic system are available [26]. The results are also valid for compressional waves [28]. Applications in the terahertz [34] and in the optical [35–37] regimes seem also possible since frequency duplicators/dividers can be used to measure the phase. Another system in which the formalism can be applied is a 1D tight-binding chain [38]. This model is ubiquitous in condensed matter [39], material science and chemistry and has several applications since the transmission and reflection coefficients can also be obtained [40]. In fact this model has realizations in chains of dielectric scatterers [41,42], in the evolution of excitations in molecular chains and in molecular rings (using nuclear magnetic resonance) [43,44]. Microwave billiards [10–12,45] and graphs [13] are also well suited to perform different tests since the applicability of

the equation to cells with more complex scatterers, as in a chain of cavities [46,47] is also possible. These kind of chains have been constructed with microwave billiards [48] and can also be constructed with thin plates [30,49]. The Heidelberg approach [50], a methodology in which the scattering matrix is built in terms of a Hamiltonian and the couplings to the exterior, is optimal for applications of Eq. (6). In fact, results of the prompt response could be possible for nuclear systems, in particular for neutron scattering, which only see the nuclei but not the electrons, would see –and identify– the periodic structure. Elastic scattering is part of nuclear reactions, and lots of data are available for (differential) cross sections and scattering of protons, electrons, or neutrons of individual nuclei. Although phase shifts are not observables, unlike cross sections, it is possible to get non univocal phase shifts from cross sections having a model (potential). Apart of other effects (as absorption, decoherence, PT-symmetric, more dimensions or a higher number of channels) that have to be included, there are many applications that could be worked out. A simple example can be thought in astrophysics: Although in supercooled neutron stars the more recent models are in favor of degenerate baryon models forming stellar superfluids [51], within the Bardeen-Cooper-Schrieffer theory, there are other models that consider crystallization in one dimension and pairing in the perpendicular planes [52].

APPENDIX A: THE NONLINEAR MAP

According to Refs. [23,27,33,53], the recurrence relation given in Eq. (5) can be interpreted as a nonlinear map for the phase of the scattering matrix. Instead of having a map for a physical variable of a single system, Eq. (5) maps the scattering matrix of a beam with $N - 1$ scatterers into the scattering matrix of a beam with N scatterers. For the phase θ of the scattering matrix the map can be written as

$$\theta_N = -\theta_{N-1} + 2 \arctan \frac{2A + (\beta - \beta^{-1})\cos(k_2 d)B - (\beta + \beta^{-1})\sin(k_2 d)D}{2C + (\beta - \beta^{-1})\cos(k_2 d)D + (\beta + \beta^{-1})\sin(k_2 d)B}, \tag{A1}$$

where

$$
\begin{aligned}
A &= \sin(k_2 d)\cos(k_2(D-d)), \\
B &= \cos(k_2(D-d))\sin(\theta_{N-1}) + \sin(k_2(D-d))\cos(\theta_{N-1}), \\
C &= \sin(k_2 d)\sin(k_2(D-d)), \\
D &= \cos(k_2(D-d))\cos(\theta_{N-1}) - \sin(k_2(D-d))\sin(\theta_{N-1}),
\end{aligned}
\tag{A2}
$$

and $\beta = (k_1 - \alpha_2 k_2/\alpha_1)/(k_1 + \alpha_2 k_2/\alpha_1)$ with α_1 and α_2 defined in Eq. (2). Examples of the dynamics of this map for

different frequencies, in the gap, within the band, and at the borders of the band, are given in Fig. 5. As it can be seen
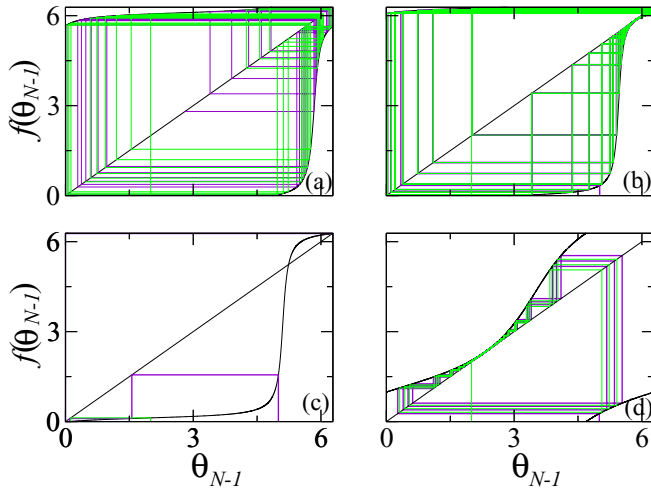
FIG. 5. Dynamics of the map given in Eq. (A1): (a) $f = 15\,000.0$, (b) $20\,272.824461676$, (c) 25180.0, and (d) $39\,735.6491631850$ Hz. The initial conditions are $\theta_0 = 2$ (green) and $\theta_0 = 5$ (purple).

in panel (c) of this figure, within the gap there are two fixed points, one stable and one unstable. The mapping shows a transition to chaos of the tangent type, see (b) and (d) in the same figure at the borders of the band. Two different values of the initial condition, i.e. the phase of the initial reflection at the border of the beam, yield similar results. The bifurcation diagram, in which the last 15 of 1000 iterations are plotted, is given in Fig. 6(a). This figure can be interpreted as the phase of the scattering matrix of 15 different beams with $N = 986, \ldots, N = 1000$. The initial condition was taken to be $\theta_0 = \pi$; other initial conditions yield similar results. As it can be seen in the bifurcation diagram, the phase shows chaotic intervals followed by intervals of stable cycles of period one. The chaotic intervals correspond to the passbands whereas the cycles of period one to the gaps. The first band starts at $f = 0$ since the beam has Neumann conditions at the
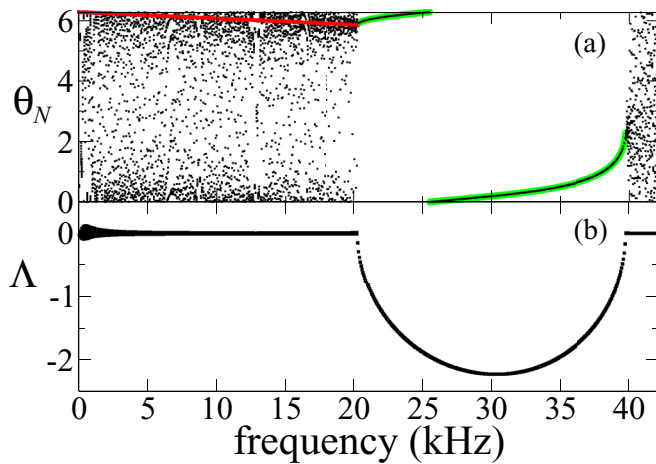
FIG. 6. (a) Bifurcation diagram of the map given in Eq. (A1). The red and green lines correspond to w_+ and θ_+. (b) Lyapunov exponent Λ calculated numerically; a very low convergence is seen at $f = 0$.
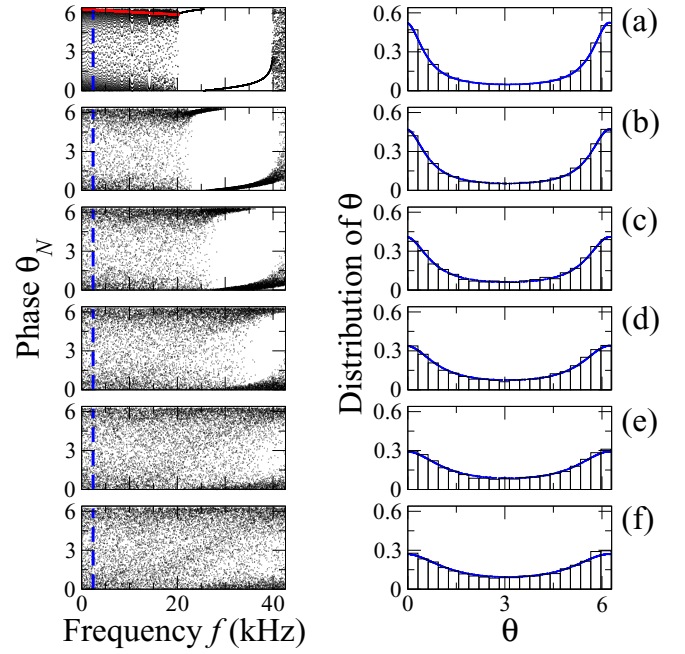
FIG. 7. (Left) The last 15 iterations, of 1000, of Eq. (5), are plotted as a function of the frequency with an initial condition $\theta_0 = \pi$ for different degrees of disorder: (a) 0%, (b) 10%, (c) 25%, (d) 50%, (e) 75%, and (f) 90%. The red line corresponds to the phase of $\langle S \rangle$ in Eq. (6); it is valid for all panels at the left because only indistinguishable changes appear. The respective histograms of the phase are given in the right panels. The continuous curve is Poisson's kernel, Eq. (1), with $\langle S \rangle$ given by Eq. (6) averaged over the disorder realizations.

boundary. In the allowed bands, the iterations of the phase cover the full interval between 0 and 2π following Poisson's kernel with $\langle S \rangle$ taken from Eq. (6), as is shown in Appendix B. The stable and unstable fixed-point solutions S_{fp} are given by [23]

$$S_{\mathrm{fp}} = \begin{cases} e^{i\theta_\pm}(f), & f \text{ in the gap}, \\ w_\pm(f), & f \text{ in the band}, \end{cases} \qquad (A3)$$

where

$$e^{i\theta_\pm}(f) = \frac{\pm\sqrt{[\mathrm{Re}\,z_n(f)]^2 - |t_n(f)|^4} + i\mathrm{Im}\,z_n(f)}{r_n^*(f)z_n(f)},$$

$$w_\pm(f) = i\frac{\pm\sqrt{|t_n(f)|^4 - [\mathrm{Re}\,z_n(f)]^2} + \mathrm{Im}\,z_n(f)}{r_n^*(f)z_n(f)},$$

and r_n and t_n are given in Eq. (4); z_n is given below Eq. (5). In Eq. (A3), $w_\pm(f)$ corresponds to the fixed-point solution of Eq. (5) extended from the unit circle to the complex plane. The phase of Eq. (A3) is also plotted in Fig. 6(a) for w_+ and θ_+.

To characterize the chaotic regions the Lyapunov exponent was calculated numerically; it is given in Fig. 6(b). As it can be seen, the Lyapunov exponent is negative in the stable cycles whereas it almost vanishes (it vanishes in the $N \to \infty$ limit [27]) in the chaotic regions.

APPENDIX B: ROBUSTNESS AGAINST DISORDER

The effect of the disorder in Eq. (6) is studied numerically varying randomly the depth of the notch with a uniform distribution of width δ. That is, the height h_2 of body 2 is varied according to $h_2 = h + \epsilon(D - h)$, where ϵ is uniformly distributed in the interval $[0, \delta]$. Thus δ quantifies the disorder strength and $\delta = 0$ corresponds to the crystalline structure. Following the analysis of Appendix A, in Fig. 7, the last 15 iterations of 1000 are plotted for different values of the disorder between 0% and 90%. As it can be seen there, the band structure is preserved for low values of the disorder strength whereas for high disorder the band structure disappears. The prediction of the optical matrix agree with the maximum of the distribution for values of the wave number in the middle of the first band whereas in the gap and in the second band high deviations are visible. The resulting distributions, for different values of the disorder strength, at a fixed frequency $f = 2395$ Hz, are shown also in Fig. 7. The distributions of the phase agree with Poisson's kernel, even for very high values of the disorder strength. This result is relevant because it shows the universality of the fluctuations against disorder. The used $\langle S \rangle$ was obtained averaging the values of r_n and t_n from the disorder.

[1] M. Fink and C. Prada, Rep. Prog. Phys. **63**, 1933 (2000).

[2] H. Feshbach, Topics in the theory of nuclear reactions, in *Reaction Dynamics*, edited by E. W. Montroll, G. H. Vineyard, M. Levy, and P. T. Matthews (Gordon and Breach, New York, 1973), p. 169.

[3] H. Feshbach, C. E. Porter, and V. F. Weisskopf, Phys. Rev. **96**, 448 (1954).

[4] T. Ericson and T. Mayer-Kuckuk, Ann. Rev. Nuclear Sci. **16**, 183 (1966).

[5] P. A. Mello and H. U. Baranger, Waves Random Media **9**, 105 (1999).

[6] P. A. Mello and N. Kumar, *Quantum Transport in Mesoscopic Systems: Complexity and Statistical Fluctuations* (Oxford University Press, New York, 2005).

[7] G. Báez, M. Cobián-Suárez, A. M. Martínez-Argüello, M. Martínez-Mares, and R. A. Méndez-Sánchez, Acta Phys. Pol. A **124**, 1069 (2013).

[8] A. M. Martínez-Argüello, M. Martínez-Mares, M. Cobián-Suárez, G. Báez, and R. A. Méndez-Sánchez, Europhys. Lett. **110**, 54003 (2015).

[9] P. W. Brouwer and C. W. J. Beenakker, Phys. Rev. B **55**, 4695 (1997).

[10] R. A. Méndez-Sánchez, U. Kuhl, M. Barth, C. H. Lewenkopf, and H.-J. Stöckmann, Phys. Rev. Lett. **91**, 174102 (2003).

[11] S. Hemmady, X. Zheng, E. Ott, T. M. Antonsen, and S. M. Anlage, Phys. Rev. Lett. **94**, 014102 (2005).

[12] U. Kuhl, M. Martínez-Mares, R. A. Méndez-Sánchez, and H.-J. Stöckmann, Phys. Rev. Lett. **94**, 144101 (2005).

[13] M. Lawniczak, S. Bauch, O. Hul, and L. Sirko, Phys. Scr. T **2012**, 014018 (2012).

[14] Y. Aurégan and V. Pagneux, Acta Acustica united with Acustica **102**, 869 (2016).

[15] A. M. Martínez-Argüello, A. Rehemanjiang, M. Martínez-Mares, J. A. Méndez-Bermúdez, H.-J. Stöckmann, and U. Kuhl, Phys. Rev. B **98**, 075311 (2018).

[16] M. Lawniczak and L. Sirko, Sci. Rep. **9**, 5630 (2019).

[17] G. López, P. A. Mello, and T. H. Seligman, Z. Phys. A **302**, 351 (1981).

[18] P. A. Mello, P. Pereyra, and T. H. Seligman, Ann. Phys. (NY) **161**, 254 (1985).

[19] W. Friedman and P. A. Mello, Ann. Phys. (NY) **161**, 276 (1985).

[20] Y. Fyodorov and D. V. Savin, Resonance scattering of waves in chaotic systems, in *The Oxford Handbook of Random Matrix Theory*, edited by G. Akemann, J. Baik, and P. Di Francesco (Oxford University Press, Oxford, New York, 2011), Chap. 34.

[21] V. A. Gopar, M. Martínez-Mares, and R. A. Méndez-Sánchez, J. Phys. A: Math. Theor. **41**, 015103 (2008).

[22] A. M. Martínez-Argüello, R. A. Méndez-Sánchez, and M. Martínez-Mares, Phys. Rev. E **86**, 016207 (2012).

[23] V. Domínguez-Rocha, R. A. Méndez-Sánchez, M. Martínez-Mares, and A. Robledo, Physica D **412**, 132623 (2020).

[24] L. A. Juárez-Villegas and M. Martínez-Mares, Quantum Rep. **2**, 107 (2020).

[25] D. J. Griffiths and C. A. Steinke, Am. J. Phys. **69**, 137 (2001).

[26] G. A. Luna-Acosta, H. Schanze, U. Kuhl, and H.-J. Stöckmann, New J. Phys. **10**, 043005 (2008).

[27] V. Domínguez-Rocha and M. Martínez-Mares, J. Phys. A: Math. Theor. **46**, 235101 (2013).

[28] A. Morales, J. Flores, L. Gutiérrez, and R. A. Méndez-Sánchez, J. Acoust. Soc. Am. **112**, 1961 (2002).

[29] J. A. Franco-Villafañe, E. Flores-Olmedo, G. Báez, O. Gandarilla-Carrillo, and R. A. Méndez-Sánchez, Eur. J. Phys. **33**, 1761 (2012).

[30] E. Flores-Olmedo, A. M. Martínez-Argüello, M. Martínez-Mares, G. Báez, J. A. Franco-Villafañe, and R. A. Méndez-Sánchez, Sci. Rep. **6**, 25157 (2016).

[31] A. Arreola-Lucas, G. Báez, F. Cervera, A. Climente, R. A. Méndez-Sánchez, and J. Sánchez-Dehesa, Sci. Rep. **9**, 1860 (2019).

[32] R. B. do Carmo and F. M. de Aguiar, Sci. Rep. **9**, 3634 (2019).

[33] M. Martínez-Mares, V. Domínguez-Rocha, and A. Robledo, Eur. Phys. J. Spec. Top. **226**, 417 (2017).

[34] S. S. Dhillon *et al.*, J. Phys. D: Appl. Phys. **50**, 043001 (2017).

[35] M. I. Tribelsky, S. Flach, A. E. Miroshnichenko, A. V. Gorbach, and Y. S. Kivshar, Phys. Rev. Lett. **100**, 043903 (2008).

[36] A. Peña, A. Girschik, F. Libisch, S. Rotter, and A. A. Chabanov, Nat. Commun. **5**, 3488 (2014).

[37] X. Cheng, X. Ma, M. Yepez, A. Z. Genack, and P. A. Mello, Phys. Rev. B **96**, 180203(R) (2017).

[38] C. Kittel, *Introduction to Solid State Physics*, 8th ed. (Wiley, N. J., 2005).

[39] F. M. Izrailev, A. A. Krokhin, and N. M. Makarov, Phys. Rep. **512**, 125 (2012).

[40] H. L. Calvo and H. M. Pastawski, Europhys. Lett. **89**, 60002 (2010).

[41] J. A. Franco-Villafañe, E. Sadurní, S. Barkhofen, U. Kuhl, F. Mortessagne, and T. H. Seligman, Phys. Rev. Lett. **111**, 170405 (2013).

[42] C. Poli, M. Bellec, U. Kuhl, F. Mortessagne, and H. Schomerus, Nat. Commun. **6**, 6710 (2015).

[43] Z. L. Mádi, B. Brutscher, T. Schulte-Herbrüggen, R. Brüschweiler, and R. R. Ernst, Chem. Phys. Lett. **268**, 300 (1997).

[44] H. M. Pastawski, G. Usaj, and P. Lewenstein, Chem. Phys. Lett. **261**, 329 (1996).

[45] H. Schanze, H.-J. Stöckmann, M. Martinez-Mares, and C. H. Lewenkopf, Phys. Rev. E **71**, 016223 (2005).

[46] T. Dittrich, B. Mehlig, H. Schanz, and U. Smilansky, Chaos Solitons Fractals **8**, 1205 (1997).

[47] G. A. Luna-Acosta, J. A. Méndez-Bermúdez, and F. M. Izrailev, Phys. Rev. E **64**, 036206 (2001).

[48] C. Dembowski, H.-D. Gräf, R. Hofferbert, H. Rehfeld, A. Richter, and T. Weiland, Phys. Rev. E **60**, 3942 (1999).

[49] B. Gèrardin, J. Laurent, A. Derode, C. Prada, and A. Aubry, Phy. Rev. Lett. **113**, 173901 (2014).

[50] G. E. Mitchell, A. Richter, and H. A. Weidenmüller, Rev. Mod. Phys. **82**, 2845 (2010).

[51] D. Page, J. M. Lattimer, M. Prakash, A. W. Steiner, Stellar superfluids, in *Novel Superfluids*, edited by K. H. Bennemann and J. B. Ketterson (Oxford University Press, 2014), Vol. 2. See also A. Gezerlis, C. J. Pethick, and A. Schwenk, Pairing and superfluidity of nucleons in neutron stars, in *Novel Superfluids*, edited by K. H. Bennemann and J. B. Ketterson (Oxford University Press, 2014), Vol. 2.

[52] T. Takatsuka and R. Tamagaki, Prog. Theor. Phys. **62**, 1655 (1979).

[53] M. Martínez-Mares and A. Robledo, Phys. Rev. E **80**, 045201(R) (2009).